

# Nanoscale

Accepted Manuscript



This is an *Accepted Manuscript*, which has been through the Royal Society of Chemistry peer review process and has been accepted for publication.

*Accepted Manuscripts* are published online shortly after acceptance, before technical editing, formatting and proof reading. Using this free service, authors can make their results available to the community, in citable form, before we publish the edited article. We will replace this *Accepted Manuscript* with the edited and formatted *Advance Article* as soon as it is available.

You can find more information about *Accepted Manuscripts* in the [Information for Authors](#).

Please note that technical editing may introduce minor changes to the text and/or graphics, which may alter content. The journal's standard [Terms & Conditions](#) and the [Ethical guidelines](#) still apply. In no event shall the Royal Society of Chemistry be held responsible for any errors or omissions in this *Accepted Manuscript* or any consequences arising from the use of any information it contains.

## ARTICLE

Cite this:  
10.1039/x0xx00000x

DOI: **Ag-Grid/Graphene Hybrid structure for Large-Scale, Transparent, Flexible Heaters**

Junmo Kang,<sup>‡ab</sup> Yonghee Jang,<sup>‡c</sup> Youngsoo Kim,<sup>d</sup> Seung-Hyun Cho,<sup>e</sup> Jonghwan Suhr,<sup>ef</sup> Byung Hee Hong,<sup>ag</sup> Jae-Boong Choi,<sup>ac\*</sup> and Doyoung Byun<sup>c\*</sup>

Received 00th January 2012,  
Accepted 00th January 2012

DOI: 10.1039/x0xx00000x

www.rsc.org/

Recently, carbon materials such as carbon nanotubes and graphene have been proposed as alternatives to indium tin oxide (ITO) for fabricating transparent conducting materials. However, the low sheet resistance and high transmittance of these carbon materials have been challenged due to the intrinsic properties of the materials. In this paper, we introduce highly transparent and flexible conductive films based on a hybrid structure of graphene and an Ag-grid. Electrohydrodynamic (EHD) jet printing was used to produce a micro-scale grid consisting of Ag lines less than 10  $\mu\text{m}$  wide. We were able to directly write the Ag-grid on a large-area graphene/flexible substrate due to the high conductivity of graphene. The hybrid electrode could be fabricated using hot pressing transfer and EHD jet printing under a non-vacuum, maskless, and low-temperature environment. The hybrid electrode offers an effective and simple route to achieving a sheet resistance as low as  $\sim 4 \Omega/\text{square}$  with  $\sim 78\%$  optical transmittance. Finally, we demonstrate that transparent flexible heaters based on the hybrid conductive films could be used in a vehicle or smart window system.

## Introduction

Indium tin oxide (ITO) is the most widely used material for fabricating transparent conducting electrodes.<sup>1</sup> Conventional ITO has been used in rigid displays, touch screens, light-emitting diodes, and solar cells because it is highly conductive and transparent. However, the high cost of indium and its brittleness and chemical instability are drawbacks in flexible electronic and photonic device applications.<sup>2</sup> One-dimensional nanostructured materials, such as metallic nanowires (mNWs)<sup>3-5</sup> and carbon nanotubes (CNTs)<sup>6-8</sup> are attractive materials for use in transparent conducting electrodes and optoelectronic devices due to their low cost and high-speed fabrication, flexibility, and high electrical conductivity and optical transparency. However, these materials also have several disadvantages.<sup>9-12</sup> First, there is typically high contact resistance at the wire-to-wire junction. Second, the density of mNWs must significantly exceed the percolation threshold for a high sheet resistance but reduce the transmittance considerably. Third, the constraints of random CNTs or metallic NW networks and their size lead to a non-uniform sheet resistance. Fourth, micrometer-wide holes within the random networks of mNWs act as non-conductive open spaces. These problems make one-dimensional materials non-ideal candidates for transparent conducting applications. Previous studies have suggested that two-dimensional graphene is a suitable

replacement for ITO.<sup>13-15</sup> In experiments, p-doped four-layer graphene films grown by chemical vapor deposition (CVD) have exhibited low sheet resistance ( $\sim 30 \Omega/\text{square}$ ) and high optical transmittance ( $\sim 90\%$ ),<sup>16</sup> which are comparable to those of ITO. However, there is a fundamental limitation in the sheet resistance of CVD graphene. Because of its polycrystalline structures and various defects (grain boundaries, ripples, wrinkles, folds, and cracks), CVD graphene exhibits poorer electrical properties than graphene produced via mechanical exfoliation of highly ordered pyrolytic graphite (HOPG).<sup>17-19</sup> Theoretically, the intrinsic and the extrinsic sheet resistance of graphene is approximately  $30 \Omega/\text{square}$ .<sup>20</sup> In addition, the chemical doping of graphene is unstable in harsh environments.<sup>21</sup> Recently, previous works have demonstrated hybrid structures via combining 2-dimensional graphene sheets with various 1-dimensional materials such as metal grid, nanowires, and carbon nanotube to obtain the low sheet resistance and high optical transmittance for replacing commercial ITO in a broad range of applications.<sup>11,19,22-26</sup>

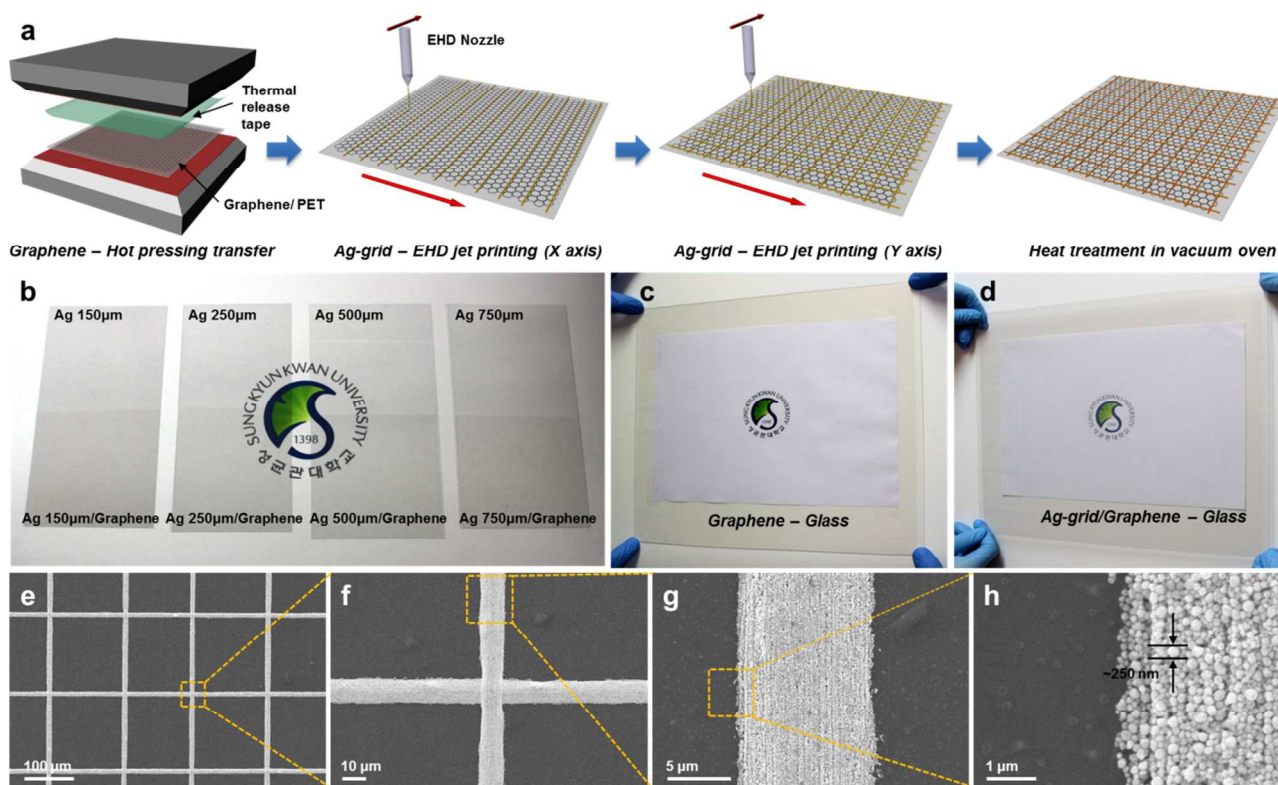
In this paper, we introduce a hybrid structure of graphene and a jet-printed Ag-grid for producing highly transparent and flexible conductive films. Using electrohydrodynamic (EHD) jet printing, Ag nanoparticle (NP) ink is directly deposited on a graphene/flexible substrate because the graphene helps to induce a strong electric field between the jet nozzle and substrate. The EHD jet-printed Ag-grid with line widths of less

than 10  $\mu\text{m}$  is rapidly fabricated on a large area substrate (18 inches along the diagonal) without a photomask or vacuum conditions. The Ag-grid provides conductive pathways through defects in the polycrystalline graphene, and the graphene provides a continuous conductive network between the Ag lines, resulting in improved electrical properties of the hybrid conductive film. Finally, we demonstrate transparent, flexible heaters using the hybrid conductive films composed of the graphene and the Ag-grid. The outstanding thermal conductivity of the graphene provides lateral heat distribution. As a result, the Ag-grid/graphene heaters exhibit a more homogeneous temperature distribution compared to the Ag-grid heaters. In addition, we characterized the mechanical flexibility of the hybrid conductive films for flexible applications, such as curved window surfaces or foldable electronic devices.

## Results and discussion

Fig. 1a illustrates the fabrication of the hybrid conductive films using hot-pressing transfer and EHD jet printing. EHD jet printing is a powerful technique for producing metal grids with line widths of a few micrometers.<sup>27,28</sup> Here, we combined this technology with a graphene dry transfer technique based on the hot-pressing method to prepare large scale transparent conducting electrodes. The hybrid conductive film fabrication process used in this study is described in the experimental

section. First, a monolayer graphene film was transferred to the target substrate using the hot-pressing method.<sup>29</sup> Then, the Ag-grids were patterned by direct writing of Ag NP ink on the graphene film via EHD jet printing. We were able to modulate the width, line-to-line distance (pitch), and thickness of the Ag lines using a self-developed software program connected to the jet printer. The software program can modulate the electric strength with hydrodynamic force control such as pumping volume and speed. We found that the line width and height of Ag lines decrease as the flow-rate decreases. Strong electrical strength could be focused line as small as 10  $\mu\text{m}$  width on a substrate with arbitrary thickness and non-conductive. The EHD jet printing technology is based on the presence of a strong electric field between the nozzle and substrate. Due to the high electrical conductivity of the graphene film, we were able to directly print the Ag-grid at a high resolution onto the film. Finally, the hybrid conductive film was subjected to heat treatment at 170°C for 2 h in a vacuum chamber to remove the chemical agents in the Ag-grid. This subsequent annealing ensures electric contact between the Ag NPs and line-line junctions, thereby creating a continuous conducting pathway on the graphene. Because this EHD jet printing is performed in air under ambient conditions and low temperatures, the technique can be applied to a flexible substrate.



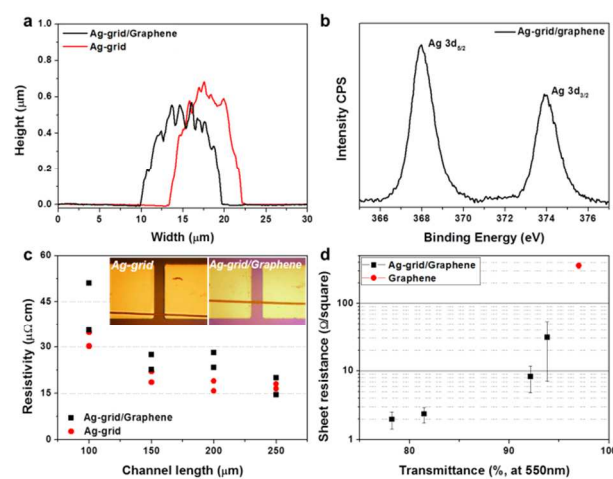
**Fig. 1** Fabrication procedures for Ag-grid and Ag-grid/graphene electrodes. (a) A schematic illustration of the Ag-grid/graphene film fabrication by hot pressing and EHD jet printing. (b) A photograph of the Ag-grid/graphene films on PET substrates. (c, d) Photographs of an 18-inch (c) graphene film and (d) Ag-grid/graphene film on glass substrates. (e-h) SEM images of the Ag-grid/graphene electrode: (e) top-view, (f) a junction between two Ag lines, (g) Ag lines on graphene film, and (h) the edge of an Ag line.

Fig. 1b presents examples of Ag-grid and Ag-grid/graphene electrodes on polyethylene terephthalate (PET) substrates (5 cm × 10 cm). The Ag-grid/graphene films appear darker than the Ag-grid films due to transfer of the monolayer graphene. The line pitch in the Ag-grids varies from 150 to 750 μm; however, the Ag-grid is invisible to the naked eye. Fig. S1† presents optical microscope images of Ag-grid and Ag-grid/graphene electrodes; no noticeable damage to the substrate is observed after the complete fabrication process. We observed that the Ag-grids were printed successfully with continuous and consistent lines on both the graphene/PET and PET substrates. We also prepared large-scale Ag-grid/graphene film on a glass substrate to demonstrate the scalability of the EHD jet printing on graphene. Figs. 1c and 1d show the large-area monolayer graphene and Ag-grid/graphene on an 18-inch-diagonal glass substrate, respectively. The microstructure of the Ag-grid on the graphene was examined using scanning electron microscopy (SEM), as shown in Figs. 1e-h. The SEM images reveal that the Ag lines are approximately 10 μm wide and the lines intersect normally at their junctions in the grid (Figs. 1f and 1g). The higher-magnification SEM image confirms that the Ag lines consist of spherical Ag NPs with an average diameter of ~250 nm after 170°C annealing (Fig. 1h).

Certain features can be observed in a transverse profile of an Ag line measured by atomic force microscopy (AFM), as shown in Fig. 2a. The height and width of the Ag line on the SiO<sub>2</sub>/Si wafer are approximately 0.6 μm and 9 μm, respectively, whereas those of the Ag line on the graphene/SiO<sub>2</sub>/Si are approximately 0.5 μm and 10 μm, respectively. The slightly lesser height of the Ag line on the graphene contributes to the slightly wider width. The effect on surface energy and conductive characteristic of substrate will be formed different width and height. Fig. S2† shows the contact angle evolution of a SiO<sub>2</sub>/Si wafer, graphene after transferred to SiO<sub>2</sub>/Si, and after annealing at 300 °C in Ar/H<sub>2</sub>. The average contact angles of graphene after transferred to SiO<sub>2</sub>/Si slightly dropped to 68.41° compared to that of a SiO<sub>2</sub>/Si wafer (76.02°). The AFM images of graphene after transferred to SiO<sub>2</sub>/Si clearly show PMMA residues on graphene, indicating that the PMMA residues on graphene are capable of influencing the surface wettability of the graphene. A clear surface of graphene is observed after annealing, resulting in that contact angle of the graphene increased to 79.47° (Fig. S2c† and S2f†). Fig. S3† presents a typical AFM three-dimensional profile of Ag-only and Ag-grid/graphene electrodes on SiO<sub>2</sub>/Si wafers. It is noticeable that the size of Ag NPs of Ag line/graphene has larger distribution, which is supposed to arise from the insufficient heat treatment for completely sintered NPs. However, the structures of both Ag electrodes are quite uniform along and across the scanned lines in the AFM images. High-resolution X-ray photoelectron spectroscopy (XPS) spectra of Ag 3d in the Ag-grid/graphene are presented in Fig. 2b. The existence of two Ag 3d peaks at 367.9 and 373.8 eV suggests the formation of metallic Ag NPs.<sup>30,31</sup> The XPS spectra reveal that the shifts of both Ag 3d<sub>5/2</sub> and Ag 3d<sub>3/2</sub> to a lower binding energy (~0.2 eV) may be due to the occurrence of electron transfer from the metallic Ag NPs to

the graphene sheet.<sup>32</sup> According to the literature,<sup>33</sup> high-resolution spectra of O 1s have provided quantitative information concerning Ag<sub>2</sub>O formation at 529.1 eV (Fig. S4c†). The element distribution was further examined by the energy dispersive spectrometer (EDS) at top and middle of Ag-grid (Fig. S5†). In air, the surface of the Ag-grid was partially oxidized. However, no oxygen element was detected in the Ag grid middle point. The XPS and EDS data indicated that no significant Ag<sub>2</sub>O peak and no oxygen element appeared in our analysis, suggesting that the graphene layer effectively contributes to the prevention of oxidation from middle to bottom of the Ag NPs by protecting the NPs from air exposure through the PET substrate.

We compared the electrical properties of the hybrid electrode to the Ag-only electrode using two-terminal conductivity measurements. For the hybrid electrode, monolayer graphene was transferred between Au electrodes and patterned using a stencil mask to fabricate the graphene-based field-effect transistor (FET). The Raman spectral data and transport measurement of the graphene FET were representative of monolayer graphene with low D peaks and a carrier mobility as great as ~4,000 cm<sup>2</sup> V<sup>-1</sup> S<sup>-1</sup>, indicating that the quality of the graphene was very high (Fig. S6†). We fabricated the Ag-only electrode and hybrid electrode between Au electrodes with 100 ~ 250-μm channel lengths. As shown in Fig. 2c, the resistivity of both the Ag-only and Ag-grid/graphene electrodes displayed negligible dependence on the channel length for lengths exceeding 150 μm. We estimated resistivity of ~20 μΩcm in the Ag-grid electrode and ~25 μΩcm in the Ag-grid/graphene electrode, which were calculated using the relationship  $\rho = R \cdot (A/l)$ , where  $l$  and  $A$  are the length and cross-sectional area, respectively, of a single Ag electrode based on the AFM data (Fig. 2a).



**Fig. 2** (a) Transverse AFM profile of Ag-grid and Ag-grid/graphene electrodes. (b) High-resolution XPS spectrum of Ag 3d peaks from an Ag-grid/graphene electrode. (c) The resistivity of the Ag-grid and Ag-grid/graphene as a function of the channel length. (d) Transmittance and sheet resistance of graphene film and Ag-grid/graphene films on PET substrates. The sheet resistance and transmittance were measured at four different positions for each Ag-grid/graphene sample.

The resistivities of the Ag-grid and Ag-grid/graphene electrodes are approximately 10 times higher than that of bulk silver, most likely due to residual solvent trapped between incompletely sintered Ag NPs, but are still sufficiently low for their use as an electrical conductor.<sup>34</sup> Fig. 2d shows a plot of the sheet resistance ( $R_s$ ) and the transmittance ( $T_r$ ) of the graphene and Ag-grid/graphene electrodes on PET substrates as a function of the grid pitch. Primarily, the  $R_s$  and  $T_r$  values of the Ag-grid/graphene electrodes are dependent on the pitch. The  $T_r$  values of the Ag-only electrodes in the visible range decrease from 97.5% to 80% as the pitch is narrowed from 750 to 150  $\mu\text{m}$  (Fig. S7†). The addition of the graphene film caused a 2-3% loss in  $T_r$  compared with the Ag-only electrodes.<sup>35</sup> However, the  $R_s$  value of the graphene is significantly enhanced after deposition of the Ag-grid. The  $R_s$  of the Ag-grid/graphene with a 500- $\mu\text{m}$  pitch is as low as  $\sim 26 \Omega/\text{square}$ , and the  $T_r$  is 92.1%, both of which represent an improvement over ITO/PET film. ( $R_s \sim 30\text{-}80 \Omega/\text{square}$  with  $\sim 90\%$  of  $T_r$ ).<sup>22</sup> Furthermore, the  $R_s$  of the 150- $\mu\text{m}$ -pitch Ag-grid/graphene is as low as  $\sim 3.8 \Omega/\text{square}$  ( $T_r$  of 78.2%), which is comparable to that of the Ag-only electrode and other transparent conductive films from previous studies.<sup>11,19,22,36</sup> The Ag-grid on the graphene provides a highly conductive pathway for charge carriers through the microstructure of graphene grain boundaries, and therefore, the  $R_s$  of the Ag-grid/graphene electrode significantly decreases.<sup>19</sup> Fig. S8† presents the  $R_s$  distribution of the large-area monolayer graphene and the Ag-grid/graphene electrodes on 18-inch-diagonal glass substrates. The large-area Ag-grid/graphene electrode exhibits an average  $R_s$  of 39.1  $\Omega/\text{square}$ , which is dramatically lower than that of the graphene-only film, which yields an average  $R_s$  of 384.7  $\Omega/\text{square}$  based on Gaussian fits.

To demonstrate the potential of the Ag-grid/graphene as a transparent flexible heater, we prepared two types of Ag-grid and Ag-grid/graphene films. The input voltage was supplied to the heaters through two-terminal side copper electrodes, which made contact with the film along its opposite edges (Fig. 3a). Fig. 3b depicts the time-dependent temperatures of the two types of heaters at an input voltage of 4 V. The temperatures of all the heaters exponentially increased from room temperature to a steady-state temperature in less than 30s. This performance is superior to that of other transparent conducting heaters.<sup>37-41</sup> This rapid heating may result from the rapid movement of electrons in the hybrid electrodes due to the high electrical conductivity of the Ag-grid and high mobility of the graphene. The steady-state temperatures of the Ag-grid/graphene heaters increased from 30°C to 145°C with decreases in the pitch from 750  $\mu\text{m}$  to 150  $\mu\text{m}$ , which is attributable to the enhanced sheet resistance of the Ag-grid/graphene film. Fig. 3c shows the steady-state temperatures of all of the heaters as a function of the applied voltage. The steady-state temperatures of the heaters gradually increased with the input voltage, whereas the slope  $^{\circ}\text{C}/\text{V}$  gradually declined as the pitch was increased from 150 to 750  $\mu\text{m}$ . It is well known that a higher temperature at a low input voltage implies the efficient transduction of electrical energy into Joule heating.<sup>38</sup> However, the inverse slope values

( $\text{W}/\text{cm}^2 \text{ } ^{\circ}\text{C}$ ) associated with the Ag-grid/graphene heaters are slightly lower than those associated with the Ag-grid film heaters, which indicates that the Ag-grid/graphene heater requires less power to obtain the same temperature than the Ag-grid heaters (Figs. 3d and S9†). It means that Ag-grid/graphene heaters could be used as transparent heaters with lower power consumption.

Although the Ag-grid heaters exhibited a higher steady-state temperature than the Ag-grid/graphene heaters with an input voltage of 4 V, the graphene layer tended to form a continuous conductive network between the Ag-grid lines, resulting in a more uniform temperature distribution (Fig. 4). The standard deviation values of temperature distribution on the Ag-grid/graphene heaters are lower than those of the Ag-grid heaters, which indicate that the graphene helped to spread the concentrated heat from the center of the Ag-grid to the graphene layer spaces. To further compare the temperature distribution in the Ag-grid/graphene heaters and the Ag-grid heaters, various input voltages (modulated from 3 V from 12 V) were supplied to the each of the heaters until a temperature of approximately 100°C was reached (Fig. S10†). The heating performance of the hybrid film is sensitive to not only Ag-grid pitch, but also the number of graphene layers. We measured the heating performance of the Ag-grid/2-layer graphene film and the results are summarized in Fig. S11†. From the measurement results, we concluded that the heat distribution of hybrid film is dependent of the layer numbers of graphene. Therefore, the Ag-grid/graphene heaters exhibited more uniform temperature distributions throughout the films than the Ag-grid heaters.

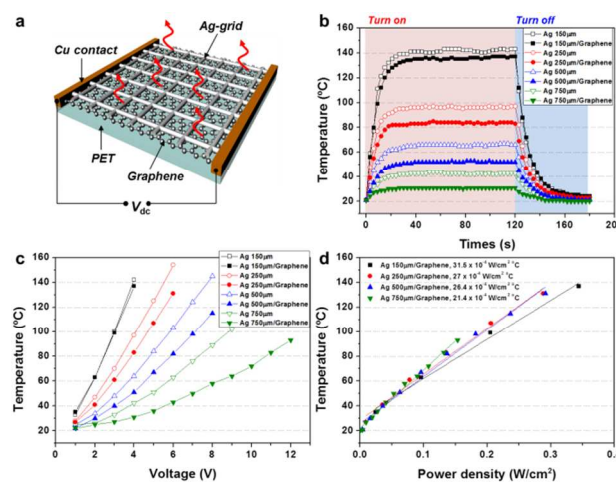


**Fig. 3** Temperature profiles of Ag-grid and Ag-grid/graphene heaters. (a) Schematic illustration of Ag-grid/graphene film heater connected to Cu electrodes. The size of the heating area was  $5 \times 5 \text{ cm}^2$ . (b) Time-dependent temperature response of Ag-grid and Ag-grid/graphene heaters. The surface temperature was monitored using an IR thermometer; the temperature responses of the heaters were measured every three seconds. (c) Steady-state temperature of Ag-grid and Ag-grid/graphene heaters as a function of the input voltage. (d) Steady-state temperatures of the Ag-grid/graphene heaters as a function of input power density.

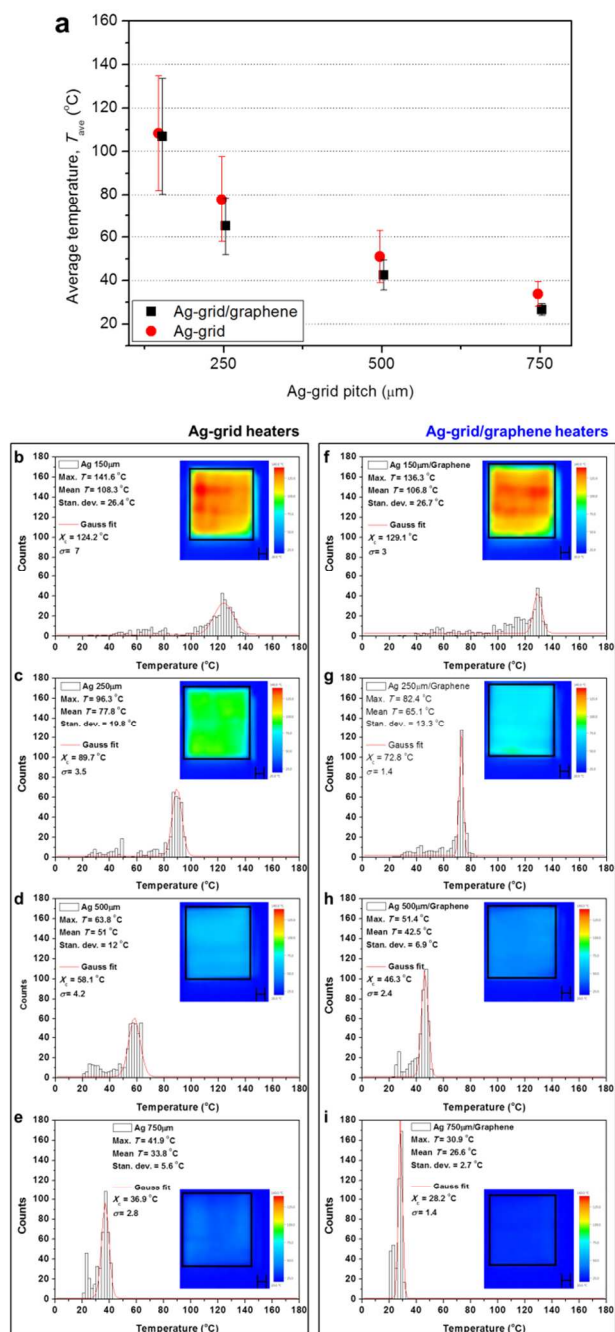


**Fig. 4** Temperature distribution of Ag-grid and Ag-grid/graphene heaters. (a) The average temperature and temperature distribution of the Ag-grid and Ag-grid/graphene heaters as a function of the grid pitch. (b-i) Statistical analysis of the temperature distribution in the (b-e) Ag-grid and (f-i) Ag-grid/graphene heaters at input voltage of 4 V. The inserted infrared images show the heaters at steady-state temperatures.

To examine the flexibility and electromechanical stability of the Ag-grid/graphene heaters, we describe the experimental results obtained by changing the temperature of the Ag-grid/graphene heaters during mechanical strain and bending cycles. Fig. 5a demonstrates the temperature variation of 150- $\mu\text{m}$ -pitch Ag-grid/graphene heater as a function of bending-induced strain. The relative differences in temperature ( $\Delta T/T_0$ ) of both the Ag-grid/graphene heater increased only  $\sim 7\%$ ,

respectively, with bending strains up to 4.2% (corresponding to a bending radius of 2.2 mm), indicating excellent flexibility. In addition to the electromechanical stability experiments, we also performed a bending stability test (Fig. 5b). The temperature of the Ag-grid/graphene did not vary significantly with up to 1,000 bending cycles. These results are comparable to the performance of previous graphene-based and other hybrid electrodes-based heaters under mechanical strain.<sup>37,38,41</sup>

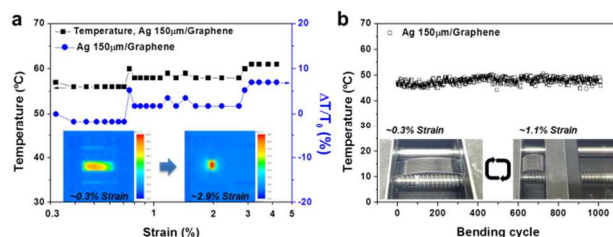


**Fig. 5** Mechanical characterizations of the 150- $\mu\text{m}$ -pitch Ag-grid/graphene heater. (a) Variations in the temperature as a function of bending strain. The inserted infrared images show the Ag-grid/graphene heater at 0.3% and 2.9% strains. (b) Mechanical stability test results of the Ag-grid/graphene heater. The bending rate was one cycle per 14 s (0.05 Hz) during application of the input voltage. The bottom inserts present photographs of the bending deformation of the Ag-grid/graphene heater at minimum (0.3%) and maximum (1.1%) strains.

## Conclusions

In this paper, we experimentally prepared an Ag-grid/graphene electrode. We fabricated a hybrid structure of graphene and an Ag-grid using hot-pressing transfer and EHD jet printing, resulting in a large-scale hybrid conductive film. This hybrid conductive film exhibited superior electrical properties and heating performance. In particular, the Ag-grid/graphene exhibited uniform heat distribution and excellent electromechanical stability. We suggest that such transparent flexible heaters based on hybrid conductive films be used in vehicles or smart window systems.

## Experimental

### Synthesis of graphene

We used hydrogen (2 sccm) and methane (20 sccm) gases to grow a high-quality graphene film. The graphene film was grown on Cu foil using the CVD method at low pressure. First, a 25- $\mu\text{m}$ -thick Cu foil was inserted into a quartz tube and heated to 970°C under  $\text{H}_2$ . The  $\text{CH}_4$  was injected into the tube to grow the graphene. The growth was allowed to proceed for 30 min, and then the tube was rapidly cooled down to room temperature. Thermal release tape (TRT, Nitto Denko) was placed on the graphene film, and then the Cu foil was chemically removed using Cu etchant (0.1M ammonia persulfate, Sigma Aldrich). The graphene on the TRT was inserted between soft rollers together with the target substrates. The TRT could be easily released after heat treatment using hot pressing.

### EHD jet printing

The Ag NPs in triethylene glycol monoethyl ether (Sigma-Aldrich) were well dispersed by stirring using a homogenizer and vortex mixer. A continuous micro-scale line was extracted using a stainless-steel nozzle with an applied electric field of 2 kV. The experiment was conducted using an EHD jet printer (NP-200, Enjet Inc.). The silver lines were patterned on the film while keeping the nozzle 2 mm above the substrate. The inner and outer diameters of the stainless steel nozzle were 100  $\mu\text{m}$  and 200  $\mu\text{m}$ , respectively. A syringe pump generated a flow rate of 150 nl/min. The Ag lines were printed at a fixed scanning speed of 30 cm/s. The EHD jet-printed Ag-grid was annealed at low pressures at 170°C for 2 h.

### Characterization

The width and thickness of the Ag lines were measured using an optical microscope, an AFM (Park system, XE-100), and an SEM (JEOL, JSM-6390). The EDS was utilized to elucidate the approximated chemical compounds for the Ag-grid on graphene/PET substrate using Hitachi X5200 SEM. Non-contact-mode AFM images were acquired at a 0.5 Hz scan rate. XPS was performed to determine the binding energy of the Ag and carbon bonding (VG Microtech ESCA2000). The sheet resistance was measured using a four-point probe with a nanovoltmeter (Keithley 6221, 2182A). An Agilent 2602 system was used to measure the graphene field-effect transistors. The transmittance was characterized by UV-vis-NIR spectroscopy (Agilent 8453). Raman spectroscopy (Renishaw, 514 nm, Ar<sup>+</sup> ion laser) was used to characterize the quality of the graphene film. The DC voltage was supplied to the hybrid conductive film heaters between copper electrodes making contact with the film along its opposite edges. The temperature of the film was measured using an infrared scanner (Testo 880).

### Acknowledgements

Thanks the support from the Basic Science Research Program through the National Research Foundation of Korea (NRF) funded by the Ministry of Education, Science and Technology (2011-0016461), the Postdoctoral Research Program of Sungkyunkwan University(2014), and Global Frontier Research Center for Advanced Soft Electronics (2011-0031629).

### Notes and references

<sup>a</sup> SKKU Advanced Institute of Nanotechnology (SAINT) and Center for Human Interface Nano Technology (HINT), Sungkyunkwan University, Suwon 440-746, Korea.

<sup>b</sup> Departments of Materials Science and Engineering, Northwestern University, Evanston, Illinois 60208, United States.

<sup>c</sup> School of Mechanical Engineering, Sungkyunkwan University, Suwon 440-746, Korea.

<sup>d</sup> Department of Physics and Astronomy, Seoul National University, Seoul, 151-742, Korea.

<sup>e</sup> Department of Polymer Science and Engineering, Sungkyunkwan University, Suwon 440-746, Korea.

<sup>f</sup> Department of Energy Science, Sungkyunkwan University, Suwon 440-746, Korea.

<sup>g</sup> Department of Chemistry, Seoul National University, Seoul 143-747, Korea.

† Online supporting information is available.

‡ These authors contributed equally to this work.

1. R. G. Gordon, *MRS bull.*, 2000, **25**, 52-57.
2. A. Kumar and C. Zhou, *ACS Nano*, 2010, **4**, 11-14.
3. D. S. Leem, A. Edwards, M. Faist, J. Nelson, D. D. Bradley and J. C. de Mello, *Adv. Mater.*, 2011, **23**, 4371-4375.
4. E. C. Garnett, W. Cai, J. J. Cha, F. Mahmood, S. T. Connor, M. G. Christoforo, Y. Cui, M. D. McGehee, M. L. Brongersma, *Nature materials* 2012, **11**, 241-249.
5. L. Hu, H. S. Kim, J.-Y. Lee, P. Peumans and Y. Cui, *ACS Nano*, 2010, **4**, 2955-2963.
6. M. Zhang, S. Fang, A. A. Zakhidov, S. B. Lee, A. E. Aliev, C. D. Williams, K. R. Atkinson and R. H. Baughman, *Science*, 2005, **309**, 1215-1219.
7. D. S. Hecht, L. Hu and G. Irvin, *Adv. Mater.*, 2011, **23**, 1482-1513.
8. B. Dan, G. C. Irvin and M. Pasquali, *ACS Nano*, 2009, **3**, 835-843.
9. J. S. Woo, J. T. Han, S. Jung, J. I. Jang, H. Y. Kim, H. J. Jeong, S. Y. Jeong, K.-J. Baeg and G.-W. Lee, *Sci. Rep.*, 2014, **4**.
10. P. N. Nirmalraj, P. E. Lyons, S. De, J. N. Coleman and J. J. Boland, *Nano Lett.*, 2009, **9**, 3890-3895.
11. M.-S. Lee, K. Lee, S.-Y. Kim, H. Lee, J. Park, K.-H. Choi, H.-K. Kim, D.-G. Kim, D.-Y. Lee and S. Nam, J. -U. Park, *Nano Lett.*, 2013, **13**, 2814-2821.
12. J.-Y. Lee, S. T. Connor, Y. Cui and P. Peumans, *Nano Lett.*, 2008, **8**, 689-692.
13. A. K. Geim and K. S. Novoselov, *Nat. Mater.*, 2007, **6**, 183-191.
14. X. Li, W. Cai, J. An, S. Kim, J. Nah, D. Yang, R. Piner, A. Velamakanni, I. Jung and E. Tutuc, S. K. Banerjee, L. Colombo, and R. S. Ruoff, *Science*, 2009, **324**, 1312-1314.
15. K. S. Kim, Y. Zhao, H. Jang, S. Y. Lee, J. M. Kim, K. S. Kim, J.-H. Ahn, P. Kim, J.-Y. Choi and B. H. Hong, *Nature*, 2009, **457**, 706-710.
16. S. Bae, H. Kim, Y. Lee, X. Xu, J.-S. Park, Y. Zheng, J. Balakrishnan, T. Lei, H. R. Kim and Y. I. Song, Y. -J. Kim, K. S. Kim. B. Özyilmaz, J. -H. Ahn, B. H. Hong, *Nat. Nano.*, 2010, **5**, 574-578.
17. P. Y. Huang, C. S. Ruiz-Vargas, A. M. van der Zande, W. S. Whitney, M. P. Levendorf, J. W. Kevek, S. Garg, J. S. Alden, C. J. Hustedt and Y. Zhu, J. Park, P. L. McEuen and D. A. Muller, *Nature*, 2011, **469**, 389-392.
18. A. W. Tsen, L. Brown, M. P. Levendorf, F. Ghahari, P. Y. Huang, R. W. Havener, C. S. Ruiz-Vargas, D. A. Muller, P. Kim and J. Park, *Science*, 2012, **336**, 1143-1146.
19. I. N. Kholmanov, C. W. Magnuson, A. E. Aliev, H. Li, B. Zhang, J. W. Suk, L. L. Zhang, E. Peng, S. H. Mousavi and A. B. Khanikaev, R. Piner, G. Shvets, R. S. Ruoff, *Nano Lett.*, 2012, **12**, 5679-5683.
20. J.-H. Chen, C. Jang, S. Xiao, M. Ishigami and M. S. Fuhrer, *Nat. Nano.*, 2008, **3**, 206-209.
21. L. Panchakarla, K. Subrahmanyam, S. Saha, A. Govindaraj, H. Krishnamurthy, U. Waghmare and C. Rao, *Adv. Mater.*, 2009, **21**, 4726-4730.

22. Y. Zhu, Z. Sun, Z. Yan, Z. Jin and J. M. Tour, *ACS Nano*, 2011, **5**, 6472-6479.
23. Zhi. Li, J. Kang, Z. Liu, C. Du, X. Lee, X. Li, L. Wang, X. Yi, H. Zhu, G. Wang, *AIP Adv.*, 2013, **3**, 042134.
24. T. L. Chen, D. S. Ghosh, V. Mkhitarian, V. Pruneri, *ACS Appl. Mater. Interfaces*, 2013, **5**, 11756-11761.
25. D. Kim, L. Zhu, D.-J. Jeong, K. Chun, Y.-Y. Bang, S.-R. Kim, J.-H. Kim and S.-K. Oh, *Carbon*, 2013, **63**, 530-536.
26. P. Dong, Y. Zhu, J. Zhang, C. Peng, Z. Yan, L. Li, Z. Peng, G. Ruan, W. Xiao, H. Lin, J. M. Tour and J. Lou, *J. Phys. Chem. C*, 2014, **118**, 25863-25868.
27. J.-U. Park, M. Hardy, S. J. Kang, K. Barton, K. Adair, D. kishore Mukhopadhyay, C. Y. Lee, M. S. Strano, A. G. Alleyne and J. G. Georgiadis, *Nat. Mater.*, 2007, **6**, 782-789.
28. Y. Jang, J. Kim and D. Byun, *J. Phys. D: Appl. Phys.*, 2013, **46**, 155103.
29. J. Kang, S. Hwang, J. H. Kim, M. H. Kim, J. Ryu, S. J. Seo, B. H. Hong, M. K. Kim and J.-B. Choi, *ACS Nano*, 2012, **6**, 5360-5365.
30. J. F. Moulder, W. F. Stickle, P. E. Sobol and K. D. Bomben, *Handbook of X-ray photoelectron spectroscopy*, Perkin Elmer Eden Prairie, MN, 1992.
31. V. K. Kaushik, *Journal of Electron Spectroscopy and Related Phenomena*, 1991, **56**, 273-277.
32. S. Chook, C. Chia, S. Zakaria, M. Ayob, K. Chee, N. Huang, H. Neoh, H. Lim, R. Jamal and R. Rahman, *Nanoscale Res. Lett.*, 2012, **7**, 541.
33. Y. Han, R. Lupitskyy, T.-M. Chou, C. M. Stafford, H. Du and S. Sukhishvili, *Analyt. Chem.*, 2011, **83**, 5873-5880.
34. S. Hong, J. Yeo, G. Kim, D. Kim, H. Lee, J. Kwon, H. Lee, P. Lee and S. H. Ko, *ACS Nano*, 2013, **7**, 5024-5031.
35. R. Nair, P. Blake, A. Grigorenko, K. Novoselov, T. Booth, T. Stauber, N. Peres and A. Geim, *Science*, 2008, **320**, 1308-1308.
36. I. K. Moon, J. I. Kim, H. Lee, K. Hur, W. C. Kim and H. Lee, *Sci. Rep.*, 2013, **3**.
37. J. Kang, H. Kim, K. S. Kim, S.-K. Lee, S. Bae, J.-H. Ahn, Y.-J. Kim, J.-B. Choi and B. H. Hong, *Nano Lett.*, 2011, **11**, 5154-5158.
38. T. Kim, Y. W. Kim, H. S. Lee, H. Kim, W. S. Yang and K. S. Suh, *Adv. Func. Mater.*, 2013, **23**, 1250-1255.
39. Y. H. Yoon, J. W. Song, D. Kim, J. Kim, J. K. Park, S. K. Oh and C. S. Han, *Adv. Mater.*, 2007, **19**, 4284-4287.
40. J. J. Bae, S. C. Lim, G. H. Han, Y. W. Jo, D. L. Doung, E. S. Kim, S. J. Chae, T. Q. Huy, N. Van Luan and Y. H. Lee, *Adv. Func. Mater.*, 2012, **22**, 4819-4826.
41. D. Sui, Y. Huang, L. Hyang, J. Liang, Y. Ma, Y. Chen Y, *Small*, 2011, **7**, 3186-3192.